

## Letter

**Visualizing Chemo-Mechanical Degradation of a Solid-State Battery Electrolyte**

Jared Tippens, John Miers, Arman Afshar, John Lewis, Francisco Javier Quintero Cortes, Haipeng Qiao, Thomas S. Marchese, Claudio V Di Leo, Christopher Saldana, and Matthew T. McDowell

ACS Energy Lett., **Just Accepted Manuscript** • DOI: 10.1021/acsenerylett.9b00816 • Publication Date (Web): 04 Jun 2019

Downloaded from <http://pubs.acs.org> on June 5, 2019

**Just Accepted**

"Just Accepted" manuscripts have been peer-reviewed and accepted for publication. They are posted online prior to technical editing, formatting for publication and author proofing. The American Chemical Society provides "Just Accepted" as a service to the research community to expedite the dissemination of scientific material as soon as possible after acceptance. "Just Accepted" manuscripts appear in full in PDF format accompanied by an HTML abstract. "Just Accepted" manuscripts have been fully peer reviewed, but should not be considered the official version of record. They are citable by the Digital Object Identifier (DOI®). "Just Accepted" is an optional service offered to authors. Therefore, the "Just Accepted" Web site may not include all articles that will be published in the journal. After a manuscript is technically edited and formatted, it will be removed from the "Just Accepted" Web site and published as an ASAP article. Note that technical editing may introduce minor changes to the manuscript text and/or graphics which could affect content, and all legal disclaimers and ethical guidelines that apply to the journal pertain. ACS cannot be held responsible for errors or consequences arising from the use of information contained in these "Just Accepted" manuscripts.

**Visualizing Chemo-Mechanical Degradation of a Solid-State Battery Electrolyte**

**AUTHORS**

Jared Tippens<sup>1</sup>, John C. Miers<sup>1</sup>, Arman Afshar<sup>3</sup>, John A. Lewis<sup>2</sup>, Francisco Javier Quintero Cortes<sup>2</sup>, Haipeng Qiao<sup>1</sup>, Thomas S. Marchese<sup>2</sup>, Claudio V. Di Leo<sup>3</sup>, Christopher Saldana<sup>1</sup>, Matthew T. McDowell<sup>1,2\*</sup>

**AFFILIATIONS**

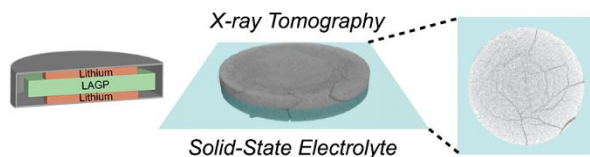
<sup>1</sup>George W. Woodruff School of Mechanical Engineering, Georgia Institute of Technology, 801 Ferst Drive, Atlanta, GA, 30332  
<sup>2</sup>School of Materials Science and Engineering, Georgia Institute of Technology, 771 Ferst Drive, Atlanta, GA, 30332  
<sup>3</sup>The Daniel Guggenheim School of Aerospace Engineering, Georgia Institute of Technology, 270 Ferst Drive, Atlanta, GA, 30332

\*Corresponding Author: [mattmcdowell@gatech.edu](mailto:mattmcdowell@gatech.edu)

## ABSTRACT

Transformations at interfaces between solid-state electrolytes (SSEs) and lithium metal electrodes can lead to high impedance and capacity decay during cycling of solid-state batteries, but the links between structural/chemical/mechanical evolution of interfaces and electrochemistry are not well understood. Here, we use *in-situ* X-ray computed tomography to reveal the evolution of mechanical damage within a  $\text{Li}_{1+x}\text{Al}_x\text{Ge}_{2-x}(\text{PO}_4)_3$  (LAGP) SSE caused by interphase growth during electrochemical cycling. The growth of an interphase with expanded volume drives fracture in this material, and the extent of fracture during cycling is found to be the primary factor causing the impedance increase, as opposed to the resistance of the interphase itself. Cracks are observed to initiate near the edge of the lithium/LAGP interface, which agrees with simulations. The chemo-mechanical effects of interphase growth studied here are expected to play a role in a variety of SSE materials, and this work is a step towards designing durable interfaces.

## TOC Graphic



**MAIN TEXT**

Solid-state batteries (SSBs) have the potential for increased energy density and improved safety compared to conventional Li-ion batteries. SSBs containing a lithium metal anode could bypass the longstanding challenges of using lithium metal in liquid-based batteries, where growth of dendrites can cause inefficient cycling and dangerous short-circuiting.<sup>1-3</sup> The solid-state electrolyte (SSE) membrane within SSBs may potentially mitigate this issue if filamentary lithium growth can be prevented.<sup>4-6</sup> Such batteries would be ideal for the electrification of ground transportation and even aviation, which requires high energy density with maximized safety and stability.

Despite the discovery of numerous highly-conductive SSE materials in recent years,<sup>7-11</sup> solid-state batteries are not yet widely commercialized. The understanding of and control over physio-chemical phenomena at the interfaces between SSEs and electrode materials remain critical issues.<sup>12,13</sup> In particular, electro-chemo-mechanical degradation driven by interfacial reactions or lithium metal filament penetration have plagued a variety of different SSB chemistries.<sup>14-18</sup> Growth of new phases between SSEs and electrode materials can result in high impedance or mechanical degradation that severely limits SSB performance, galvanizing research efforts to understand the problem in greater detail.<sup>14,19-23</sup>

For several ceramic oxide and sulfide electrolytes, lithium metal filaments have been found to grow through the SSE when cycled at current densities greater than critical values, resulting in short-circuiting of cells.<sup>15-18</sup> However, a different degradation mechanism has been observed for certain NASICON-type SSEs. NASICON materials are advantageous for SSB applications due to their relatively high ionic conductivity,<sup>24-26</sup> as well as their good chemical stability against moisture, air, and some cathodes.<sup>22,27,28</sup> A key challenge with NASICONs and

many other SSEs is their instability in contact with lithium metal,<sup>29,30</sup> and the growth of an ‘interphase’ region due to the direct (electro)chemical reaction between the SSE and lithium metal can drive premature chemo-mechanical degradation of the SSB.<sup>14,31</sup> This has recently been investigated for the NASICON material  $\text{Li}_{1+x}\text{Al}_x\text{Ge}_{2-x}(\text{PO}_4)_3$  (LAGP), where the growth of an interphase layer is thought to cause mechanical fracture.<sup>14,30</sup> Through *in-situ* transmission electron microscopy (TEM) and other experiments, our recent work showed that the reaction between LAGP and lithium involves amorphization and volume expansion. The morphology of the reacted interphase was found to be highly dependent on current density, with higher currents causing greater nonuniformity of the interphase.<sup>14</sup> While mechanical degradation has been observed post-mortem, little is known regarding the relationship between interphase formation and chemo-mechanical degradation of SSBs throughout electrochemical cycling. While cathode/SSE interfaces have also been examined,<sup>32</sup> the significant instabilities of most SSE materials in contact with lithium necessitate investigation. Improved understanding of interfacial evolution and chemo-mechanical phenomena could enable the protection and passivation of the wide variety of different SSEs with unstable interfaces for use in SSBs with lithium metal anodes.

X-ray computed tomography (CT) at the micro- and nanoscale has previously been used to probe morphological evolution of battery electrode materials primarily in liquid-electrolyte-based lithium batteries.<sup>33-39</sup> X-ray CT produces two-dimensional projection images of objects at multiple angles of incidence, which can then be used to construct a three-dimensional rendering of portions of electrodes or of full battery cells. Several previous studies have quantified chemo-mechanical degradation and fracture processes in battery electrode materials and have linked these processes to electrochemical behavior,<sup>38,39</sup> and others have used CT to observe morphological changes in

SSBs.<sup>40,41</sup> However, the potential of *in-situ* X-ray CT for probing chemo-mechanical degradation processes in SSBs has not been fully realized.

Here, we use *in-situ* X-ray micro CT to visualize fracture processes and interphase growth in LAGP solid electrolytes during cycling of symmetric solid-state cells, which enables us to directly correlate electrochemical behavior to mechanical degradation. Three-dimensional CT datasets were collected at different times during electrochemical cycling, and they reveal how the continuous growth of an interphase at the lithium/LAGP interface causes initiation and propagation of cracks within the bulk of the SSE. Fracture of the SSE is found to be directly responsible for impedance increases during cycling, contrasting with the general view that interphase layers themselves are the principal source of increased impedance. Finite element modeling shows that stress concentrations arise at the edge of the reacted interphase, which correlates with the experimentally-identified fracture initiation points. Additionally, the observed web-like crack network within the SSE is driven by the spatial variation of the different predicted stress components. This work directly demonstrates that interfacial chemical instabilities can have significant effects on the mechanical degradation of solid electrolytes, and the insight into degradation processes herein sets the stage for engineering improved solid-state batteries.

In these experiments, symmetric lithium/LAGP/lithium coin cells were constructed and electrochemically cycled within a lab-scale CT instrument. LAGP was synthesized through a sol-gel process,<sup>42</sup> resulting in a single-phase material with a rhombohedral crystal lattice (Supporting Fig. S1) and typical ionic conductivity between 0.1 and 0.3 mS cm<sup>-1</sup> (Fig. S2). Figure 1a shows a schematic of the X-ray CT experimental setup, in which the coin cell was rotated 360° while projection images were collected. The Experimental Methods section in the SI contains detailed experimental information related to electrochemical tests, CT experiments, and tomographic

reconstruction. In the configuration used here, CT imaging enables the differentiation of the solid electrolyte pellet from the lithium electrodes and the steel casing of the cell due to local contrast differences. Figure 1b shows a 3D rendering of a pristine 8.6 mm diameter LAGP pellet within a symmetric lithium/LAGP/lithium cell before cycling, and Fig. 1c shows the same pellet after electrochemical cycling for 35 hours (cycling data is shown in Fig. S3). The pellet was damage-free before cycling, while there is clear evidence of fracture after cycling. A voxel dimension of  $18.9\text{ }\mu\text{m}$  was achieved in these experiments; this resolution is lower than nano-CT and synchrotron measurements,<sup>43</sup> but micro CT enables imaging of the full cell, which is critical for mapping global mechanical degradation of the entire SSE.

To understand the evolution of the SSE morphology during battery cycling, *in-situ* experiments were performed. Figure 2a shows the electrochemical data from a symmetric cell over the course of a 52 h experiment. The cell was first cycled galvanostatically with current densities that were periodically increased from  $0.10\text{ mA cm}^{-2}$  to  $0.28\text{ mA cm}^{-2}$ . After 32 h, the overpotential started to increase rapidly, prompting a switch to potentiostatic control to avoid operating at excessive cell voltages. The cell was then cycled at progressively larger voltages from 1.5 V to 4.0 V in 4-hour increments until testing concluded. After each set of two cycles (4 h of total cycling), the electrochemical test was paused and a CT scan was conducted to render a 3D image of the LAGP. Figure 2b shows one-voxel-thick horizontal slices extracted from the center of the SSE pellet at different times during the experiment. Fracture is observed in the form of dark lines within the high-contrast LAGP. The cracks are visible in these CT slices since X-ray imaging contrast is highly dependent on density, and the absence of material within the cracks leads to lower density. The temporal evolution of the crack network is shown in Fig. 2c; these images of the crack network were generated by filtering all 2D slices of the pellet through a trainable binary segmentation

algorithm, then re-stacking them into a 3D volume. We emphasize that Fig. 2b only shows one horizontal slice from the cracked SSE, whereas Fig. 2c shows the crack network through the entire thickness of the pellet. Several pre-existing pores exist in Fig. 2c(i), which are consistently visible throughout the experiment. Fracture was first visible after 24 h of galvanostatic cycling (Fig. 2c(ii)). Figure 2c(ii) reveals two separate cracks extending radially from the interior of the pellet to the perimeter. These cracks were observed to extend through the thickness of the LAGP pellet, parallel to the direction of  $\text{Li}^+$  transport. Additional radial cracks initiated near the edge of the pellet as cycling progressed, and each of these cracks lengthened and thickened with further cycling (Fig. 2c(iii-v)). Circumferential cracks also formed, branching out from these radial cracks closer to the center of the LAGP pellet to create the interwoven web pattern shown in Fig. 2c(iii-v). In the data in Fig. 2b and c, the area close to the edge of the pellet underwent significantly less damage than the pellet interior. This is because the lithium metal electrodes only contacted 75% of the surface area and did not contact the outer edge of the LAGP. This suggests that the interfacial interaction between the lithium and LAGP is correlated with crack formation.

The segmented data in Fig. 2c also enabled quantification of the total crack volume and the quantity of cracks within the LAGP pellet during cycling. The increase in crack volume between scans is notated in Fig. 2c in  $\text{mm}^3$ , and Table S1 and Fig. S4 contain complete crack volume and quantity data from the experiment. The greatest number of new cracks was observed between 28 and 32 h of cycling (the scan in Fig. 2c(iii)), while the crack volume increased continuously after this even though fewer additional cracks formed. Thus, the crack volume increased early in the experiment largely due to the formation of new cracks, while the continued increase of crack volume later in the experiment was due both to the formation of new cracks and to the widening and lengthening of already-existing cracks.



Additional experiments were carried out to investigate the interphase that forms due to the (electro)chemical reaction between lithium and the LAGP. We note that the electrochemical growth of this interphase is likely the preferred reaction process in contrast to direct lithium plating under the experimental conditions employed here, but it is difficult to deconvolute the two possible processes. To detect the formation of an interphase layer, we constructed a symmetric cell and cycled it at lower currents ( $0.1 \text{ mA cm}^{-2}$ , Fig. S5) to allow for the growth of a thicker, uniform interphase. CT scans were conducted before and after this *ex-situ* experiment. Figure 3a shows cross-sectional images of a portion of the same slice within this pellet before and after electrochemical testing. The SSE was fractured after this process, and it is clear from the image that the top and bottom surfaces of the LAGP pellet were transformed. After cycling, the surface regions exhibited a darker contrast due to the intermediate density of the reacted interphase, which was expected since the reacted interphase forms via a conversion-like reaction and incorporation of a significant amount of lithium.<sup>14,31</sup> The plot in Fig. S6 shows the normalized image intensity across the interphase region averaged over multiple areas of the pellet; the interphase is between  $\sim 50$  and  $\sim 90 \text{ }\mu\text{m}$  thick. While the interphase formed as a uniform layer in the experiment in Fig. 3a, this was not the case for the *in-situ* experiments in Fig. 2 in which the cell was subjected to larger current densities. In these cases, a thick uniform interphase layer was not visible, and the interphase likely grew into the pellet in a non-uniform fashion. Figure 3b shows a representative cross-sectional scanning electron microscopy (SEM) image from a symmetric LAGP/lithium/LAGP cell that was cycled galvanostatically at  $0.2 \text{ mA cm}^{-2}$  until failure. The interphase appears as the region with darker contrast at the top of the LAGP pellet. It is the growth of this expanded interphase that likely induces stress and fracture in the SSE. We note that the continuous growth of the width of cracks in Fig. 2 is likely driven by the continuous expansion of

the interphase; once a crack forms, it widens and becomes more visible. SEM imaging such as that in Fig. 3b also confirmed that none of the cracks contained lithium metal.

To understand how crack propagation and impedance are related, a separate *in-situ* experiment was conducted, with electrochemistry shown in Fig. S3. Electrochemical impedance spectroscopy (EIS) showed that the overall cell impedance increased significantly (175-fold) during cycling. Figure 3c shows the impedance of this cell as a function of the total charge transferred during the experiment, which does not track directly with time since current or cell voltage was changed throughout. Full EIS data from the different experiments herein are shown in Figs. S7 and S8. Along with the cell impedance, Fig. 3c also contains a metric representing the extent of fracture (“damaged area”) within the SSE as a function of total charge transferred. The damaged area was evaluated by examining multiple cross-sections of the SSE pellet from a given CT scan and determining the fraction of the total width of each cross-section that was traversed by visible cracks (see Experimental Methods in the SI and Fig. S9 for details). Thus, the “damaged area” metric is an estimate of the fraction of the SSE area that features cracks that would inhibit Li-ion transport. As shown in Fig. 3c, the cell impedance rose only slightly during the early part of this experiment, during which no visible cracks formed. When fracture was first detected in the SSE after ~2.2 mAh of charge transferred, the impedance increased noticeably from 2.81 k $\Omega$  cm<sup>2</sup> to 6.80 k $\Omega$  cm<sup>2</sup>. As the crack network continued to grow, as measured by the damaged area in Fig. 3c, the impedance significantly increased. At the conclusion of the experiment, the impedance had risen to ~256 k $\Omega$  cm<sup>2</sup> and the damaged area was measured to be 72.4%. The pellet was likely even more fractured than this metric indicates, since cracks smaller than the resolution limit could exist that were not detected, and cracks close to the lithium/LAGP interface were also difficult to image.

The strong correlation between the damaged area and cell impedance shown in Fig. 3c indicates that electrochemical failure of these cells was due to mechanical fracture, which impedes  $\text{Li}^+$ -ion transport. Ion transport could be influenced both by the increasing quantity of cracks as well as by the increasing volume of voided fracture regions, resulting in loss of contact. Moreover, the lack of a significant increase in impedance prior to crack initiation in Fig. 3c indicates that the interphase does not hinder ionic and/or electronic transport, as the interphase is likely a mixed ion-electron conductor. Importantly, separate experiments showed that the interphase that forms before fracture with these electrochemical conditions is  $\sim 25\ \mu\text{m}$  thick (Fig. S10). In this material, therefore, it is not the transport properties of the interphase that drive electrochemical degradation; instead, it is the chemo-mechanical expansion process that governs fracture and global cell degradation.

Further analysis of crack patterns and stress evolution within the SSE was undertaken to pinpoint the origin of fracture. In the *in-situ* experiment discussed in Fig. 3c, fracture was first detected after 22 hours of cycling. Similar to the prior experiment in Fig. 2, fracture progressed throughout cycling, and the final CT scan revealed a crack network spread throughout the SSE pellet. Figure 3d(i) and (ii) show different cross-sectional slices of this LAGP pellet after cycling; these slices are oriented as shown by the dashed lines in the top-down schematic of the pellet in Fig. 3d(iii). The cross sections show that large cracks exist near the surface at the right side of the pellet and extend in various directions. The progression of fracture over the course of cycling at these two locations is shown in Fig. S11, and it is evident from this analysis that these large cracks initiated at the top surface of the pellet after  $\sim 22\ \text{h}$  of cycling. This location at the top surface of the pellet corresponds to the edge of the lithium contact region, as shown by the artificial gray shading on the outlined pellet in Fig. 3d(iii). This mapping of lithium was possible because the

lithium electrodes were directly visible in the X-ray images (Fig. S12). It is therefore clear that the cracks initiated near the edge of the lithium/LAGP contact area, and that some of the thickest visible cracks extended from this region.

To examine the links between interphase formation and fracture during cycling, finite element analysis (FEA) was used to simulate the evolution of stresses due to the dynamic formation of the interphase region. We employ a coupled diffusion-deformation model based on prior work<sup>44</sup> that incorporates species diffusion concurrent with volume expansion, plastic deformation in the reacted interphase, and stress generation. Related finite element methods have been used to model reaction processes in a variety of large-volume-change battery electrode materials.<sup>44-50</sup> A reaction front of nanoscale dimension separates the pristine LAGP from the reacted interphase, as is evident in the SEM image in Fig. 4a. Rather than modeling the complex physics associated with the formation and propagation of this reaction front, we prescribe the location of the interface through the use of spatially-varying diffusivity (see SI for details). The reacted interphase region is then prescribed to expand and flow plastically, while we model the effects of volume expansion on stress generation throughout the pellet. In these simulations, the maximum volume expansion of the reacted interphase was 130%, as measured from the chemically-reacted interphase from post-mortem SEM (Fig. 4a). A Young's modulus of 115 GPa was used for the unreacted LAGP, which is a value that has been measured for the similar NASICON material  $\text{Li}_{1.3}\text{Al}_{0.3}\text{Ti}_{1.7}(\text{PO}_4)_3$ .<sup>51</sup> Other materials properties (e.g., yield stress and Young's modulus of the reacted interphase) have not been measured, but were estimated as shown in the SI. Sensitivity analyses were undertaken and showed that moderately varying these parameters did not alter our conclusions. A full description of these simulations is provided in the SI, including Figs. S13-S15.

This model was used to simulate the interphase formation process and its effect on mechanical stress evolution. Due to the symmetry of the experiment, the problem was modeled as a two-dimensional axisymmetric disc. Figure 4b presents the simulation output showing the reaction coordinate  $c \in [0,1]$  (which is related to concentration) at the same magnification as the SEM image of the edge of the reacted interphase in Fig. 4a, showing general agreement between the shapes of the evolved interphase region in the simulation and experiment. The different stress components (radial stress  $\sigma_{rr}$ , circumferential stress  $\sigma_{\theta\theta}$ , and axial stress  $\sigma_{zz}$ ) were tracked as the interphase evolved. As shown in Fig. 4c, tensile circumferential stress would cause radial cracks to form, and tensile radial stress would cause circumferential cracks to form. Figures 4d and e show contours of the radial stress  $\sigma_{rr}$  and circumferential stress  $\sigma_{\theta\theta}$ , respectively. We note that only positive stress values are displayed here, as these would be responsible for crack formation and propagation. Areas shown in black have negative stress values, and the reacted interphase region therefore experiences compressive stress. Figure 4d and e show that there are tensile stress concentrations in  $\sigma_{rr}$  and  $\sigma_{\theta\theta}$  within the unreacted LAGP near the edge of the reacted interphase region. The position of the peak value of  $\sigma_{\theta\theta}$  (Fig. 4e) corresponds to the experimentally-observed initiation location of the radial cracks that extend to the edge of the pellet, as shown in Fig. 3d. Figure 4d shows that the region underneath the reacted interphase experiences tensile radial stress  $\sigma_{rr}$ , while the region near the edge of the LAGP pellet away from the reacted interphase is under compression. This indicates that circumferential cracks should occur only beneath the reacted interphase and not near the edge of the LAGP. The experimental crack pattern in Fig. 4c confirms this prediction, as circumferential cracks are found only beneath the lithium contact area. In contrast, Fig. 4e shows that the circumferential stress  $\sigma_{\theta\theta}$  is positive throughout much of the simulation domain, indicating that radial cracks can grow even to the extreme edge of the pellet.

This too agrees with the experimental results (Fig. 4c), where radial cracks in the LAGP propagate from the edge of the interphase region throughout the pellet, including to the pellet's perimeter. Figure S16 shows similar results for the axial stress  $\sigma_{zz}$ . The axial stress is concentrated directly beneath the entire width of the reacted interphase, indicating that horizontal cracking and delamination can occur between the reacted interphase and the pristine LAGP. It is hypothesized that such horizontal cracks can significantly influence impedance because they would directly block  $\text{Li}^+$  transport. Finally, Fig. 4f shows the evolution of  $\sigma_{\theta\theta}$  at different times during the growth of the interphase region. The circumferential stress is concentrated near the edge of the reacted interphase beginning at early times during the reaction process, and the magnitude of tensile stress increases throughout the LAGP as the reacted interlayer increases in thickness. This result again supports the observation that cracks initiated at the edge of the reacted interphase, regardless of when the cracks initiate. We note that the visible pores in the LAGP did not seem to participate in crack formation; other smaller defects may have played a role in stress intensification.

The temporal evolution of stress and the locations of maximum stress predicted by these simulations are in good agreement with the experimentally-observed evolution of fracture patterns. It is important to note that the simulations in Fig. 4 are useful for providing an understanding of where cracks could initiate and propagate. They cannot fully determine the experimental crack patterns, as the crack formation process itself will alter the stress field, and the simulations also do not account for crack initiation at flaws. Furthermore, the stress values shown in Fig. 4 depend on the materials properties used (some of which were estimated), and these values should thus be treated qualitatively. Comprehensive sensitivity analyses are presented in SI Figs. S17-S22, and they show that variation of most estimated parameters did not significantly impact stress magnitudes, while a few (such as the yield strength of the reacted interphase) had a more noticeable

1  
2  
3 effect on stress magnitude. Importantly, however, the sensitivity analysis shows that variation of  
4 these parameters does not significantly affect the spatial distribution of stresses within the LAGP.  
5  
6 Thus, the property estimates herein are sufficient for capturing the fundamental aspects of stress  
7 evolution in these experiments, while future measurement of materials properties in this and other  
8 systems will enable more precise numerical estimates of stress values. As a final note, the reacted  
9 interphase region in the experiments could be more non-uniform than that used in the simulations,  
10 but the global stress evolution should remain similar due to the overall expansion near the interface  
11 region.  
12  
13  
14  
15  
16  
17  
18  
19  
20  
21

22 Together, these experiments and simulations provide important insight into how interphase  
23 growth controls stress evolution and mechanical degradation of LAGP, with important  
24 implications for the wide variety of SSE materials that have unstable interfaces and experience  
25 interphase growth. The growth of the crack network within LAGP during cycling was observed to  
26 strongly correlate with increases in impedance. Additionally, fracture initiated at the edges of the  
27 lithium/LAGP contact area, and this finding was supported by simulations that predicted stress  
28 evolution and stress concentrations during the growth of the interphase region. Based on these  
29 results, it is clear that the interfacial reaction between lithium and LAGP drives chemo-mechanical  
30 degradation in this material. These findings also show that the growth of the interphase itself does  
31 not significantly hinder ionic and/or electronic transport, but it is the cracks that result from the  
32 growth of the interphase that drive the chemo-mechanical degradation process. An important  
33 implication of this study is that completely preventing interphase formation may not be necessary  
34 to effectively stabilize various lithium/SSE interfaces. Instead, if the interphase still allows for  $\text{Li}^+$   
35 transport, then control over the structure and morphology of the reacted interphase region, and  
36 therefore stress evolution, could be sufficient to prevent mechanical fracture and thus  
37  
38  
39  
40  
41  
42  
43  
44  
45  
46  
47  
48  
49  
50  
51  
52  
53  
54  
55  
56  
57  
58  
59  
60

electrochemical degradation. To prevent large stresses from developing, however, the interphase growth must be limited to a certain thickness through either natural or artificial means, and engineering the interface so that the interphase morphology is non-planar may also be beneficial for reducing stress concentrations.

This study underscores the importance of understanding the effects of interfacial phenomena on the coupled electro-chemo-mechanical behavior of SSEs. The vast majority of SSEs are thermodynamically unstable in contact with lithium metal,<sup>20,22</sup> but the reaction kinetics and morphological/structural evolution at the interface will determine degradation pathways. It is thus critical to gain an understanding of these phenomena, and this work shows the capabilities of *in-situ* X-ray micro-CT experiments to visualize and understand morphological changes in SSBs with lithium metal anodes. This knowledge is important for engineering lithium/SSE interfaces to minimize stress build-up, which can cause fracture that blocks Li-ion transport. Combining such knowledge with information across length scales from other techniques, such as synchrotron X-ray CT and TEM, will be critical to understand the relationship between interfacial instabilities, stress evolution, and filamentary growth of lithium within a variety of SSEs for use in high-energy solid-state batteries.

## SUPPORTING INFORMATION

The Supporting Information is available free of charge on the ACS Publications website. The SI contains full descriptions of the experimental methods, modeling methods, and additional data.

## AUTHOR INFORMATION

Corresponding author email: mattmcdowell@gatech.edu



ORCID – Matthew T. McDowell: 0000-0001-5552-3456

Notes: the authors declare no competing financial interests.

## ACKNOWLEDGMENTS

This material is based upon work supported by the National Science Foundation under Award No. DMR-1652471 and No. CMMI-1825640/1254818. This work was performed in part at the Georgia Tech Institute for Electronics and Nanotechnology, a member of the National Nanotechnology Coordinated Infrastructure, which is supported by the National Science Foundation (Grant ECCS-1542174). J.T. acknowledges the G. W. Woodruff School of Mechanical Engineering at Georgia Tech for funding support. C.V.D.L. acknowledges funding from the National Science Foundation under Award No. CMMI-1825132.

## REFERENCES

- 1 V. Etacheri, R. Marom, R. Elazari, G. Salitra & D. Aurbach. Challenges in the development of advanced Li-ion batteries: A review. *Energy Environ. Sci.* **2011**, 4 (9), 3243-3262.

- 1  
2  
3 2 B. D. McCloskey. Attainable gravimetric and volumetric energy density of Li–S and Li  
4 ion battery cells with solid separator-protected Li metal anodes. *J. Phys. Chem. Lett.*  
5  
6 **2015**, 6 (22), 4581-4588.
- 7  
8  
9  
10 3 J. Li, C. Ma, M. Chi, C. Liang & N. J. Dudney. Solid electrolyte: The key for high-  
11  
12 voltage lithium batteries. *Adv. Energy Mater.* **2015**, 5 (4), 1401408.
- 13  
14 4 C. Monroe & J. Newman. The impact of elastic deformation on deposition kinetics at  
15  
16 lithium/polymer interfaces. *J. Electrochem. Soc.* **2005**, 152 (2), A396-A404.
- 17  
18  
19 5 Z. Zhang, Y. Shao, B. V. Lotsch, Y.-S. Hu, H. Li, J. Janek, C. Nan, L. Nazar, J. Maier &  
20  
21 M. Armand. New horizons for inorganic solid state ion conductors. *Energy Environ. Sci.*  
22  
23 **2018**, 11, 1945-1976.
- 24  
25  
26 6 K. Kerman, A. Luntz, V. Viswanathan, Y.-M. Chiang & Z. Chen. Practical challenges  
27  
28 hindering the development of solid state Li ion batteries. *J. Electrochem. Soc.* **2017**, 164  
29  
30 (7), A1731-A1744.
- 31  
32  
33 7 E. Rangasamy, Z. Liu, M. Gobet, K. Pilar, G. Sahu, W. Zhou, H. Wu, S. Greenbaum &  
34  
35 C. Liang. An iodide-based Li<sub>7</sub>P<sub>2</sub>S<sub>8</sub>I superionic conductor. *J. Am. Chem. Soc.* **2015**, 137  
36  
37 (4), 1384-1387.
- 38  
39  
40 8 K. Takada. Progress and prospective of solid-state lithium batteries. *Acta Mater.* **2013**, 61  
41  
42 (3), 759-770.
- 43  
44  
45 9 A. Sakuda, A. Hayashi & M. Tatsumisago. Sulfide solid electrolyte with favorable  
46  
47 mechanical property for all-solid-state lithium battery. *Sci. Rep.* **2013**, 3, 2261.
- 48  
49  
50 10 Y. Kato, S. Hori, T. Saito, K. Suzuki, M. Hirayama, A. Mitsui, M. Yonemura, H. Iba &  
51  
52 R. Kanno. High-power all-solid-state batteries using sulfide superionic conductors. *Nat.*  
53  
54 *Energy* **2016**, 1 (4), 16030.
- 55  
56  
57  
58  
59  
60

- 1  
2  
3  
4  
5  
6  
7  
8  
9  
10  
11  
12  
13  
14  
15  
16  
17  
18  
19  
20  
21  
22  
23  
24  
25  
26  
27  
28  
29  
30  
31  
32  
33  
34  
35  
36  
37  
38  
39  
40  
41  
42  
43  
44  
45  
46  
47  
48  
49  
50  
51  
52  
53  
54  
55  
56  
57  
58  
59  
60
- 11 R. Murugan, V. Thangadurai & W. Weppner. Fast lithium ion conduction in garnet-type  $\text{Li}_7\text{La}_3\text{Zr}_2\text{O}_{12}$ . *Angew. Chem. Int. Ed.* **2007**, 46 (41), 7778-7781.
- 12 A. C. Luntz, J. Voss & K. Reuter. Interfacial challenges in solid-state Li ion batteries. *J. Phys. Chem. Lett.* **2015**, 6 (22), 4599-4604.
- 13 V. Augustyn, M. T. McDowell & A. Vojvodic. Toward an atomistic understanding of solid-state electrochemical interfaces for energy storage. *Joule* **2018**, 2 (11), 2189-2193.
- 14 J. A. Lewis, F. J. Q. Cortes, M. Boebinger, J. Tippens, T. S. Marchese, N. P. Kondekar, X. Liu, M. Chi & M. McDowell. Interphase morphology between a solid-state electrolyte and lithium controls cell failure. *ACS Energy Lett.* **2019**, 11 (2), 591-599.
- 15 Y. Ren, Y. Shen, Y. Lin & C.-W. Nan. Direct observation of lithium dendrites inside garnet-type lithium-ion solid electrolyte. *Electrochem. Commun.* **2015**, 57, 27-30.
- 16 E. J. Cheng, A. Sharafi & J. Sakamoto. Intergranular Li metal propagation through polycrystalline  $\text{Li}_{6.25}\text{Al}_{0.25}\text{La}_3\text{Zr}_2\text{O}_{12}$  ceramic electrolyte. *Electrochim. Acta* **2017**, 223, 85-91.
- 17 L. Porz, T. Swamy, B. W. Sheldon, D. Rettenwander, T. Frömling, H. L. Thaman, S. Berendts, R. Uecker, W. C. Carter & Y. M. Chiang. Mechanism of lithium metal penetration through inorganic solid electrolytes. *Adv. Energy Mater.* **2017**, 7 (20), 1701003.
- 18 F. Han, A. S. Westover, J. Yue, X. Fan, F. Wang, M. Chi, D. N. Leonard, N. J. Dudney, H. Wang & C. Wang. High electronic conductivity as the origin of lithium dendrite formation within solid electrolytes. *Nat. Energy* **2019**, 4, 187-196.

- 1  
2  
3 19 S. Wenzel, S. Randau, T. Leichtweiß, D. A. Weber, J. Sann, W. G. Zeier & J. r. Janek.  
4  
5 Direct observation of the interfacial instability of the fast ionic conductor  $\text{Li}_{10}\text{GeP}_2\text{S}_{12}$  at  
6  
7 the lithium metal anode. *Chem. Mater.* **2016**, 28 (7), 2400-2407.  
8  
9  
10 20 Y. Zhu, X. He & Y. Mo. First principles study on electrochemical and chemical stability  
11  
12 of solid electrolyte–electrode interfaces in all-solid-state Li-ion batteries. *J. Mater. Chem.*  
13  
14 *A* **2016**, 4 (9), 3253-3266.  
15  
16  
17 21 W. D. Richards, L. J. Miara, Y. Wang, J. C. Kim & G. Ceder. Interface stability in solid-  
18  
19 state batteries. *Chem. Mater.* **2015**, 28 (1), 266-273.  
20  
21  
22 22 Y. Zhu, X. He & Y. Mo. Origin of outstanding stability in the lithium solid electrolyte  
23  
24 materials: Insights from thermodynamic analyses based on first-principles calculations.  
25  
26 *ACS Appl. Mater. Inter.* **2015**, 7 (42), 23685-23693.  
27  
28  
29 23 X. Han, Y. Gong, K. K. Fu, X. He, G. T. Hitz, J. Dai, A. Pearse, B. Liu, H. Wang & G.  
30  
31 Rubloff. Negating interfacial impedance in garnet-based solid-state Li metal batteries.  
32  
33 *Nat. Mater.* **2017**, 16 (5), 572-579.  
34  
35  
36 24 M. Zhang, K. Takahashi, N. Imanishi, Y. Takeda, O. Yamamoto, B. Chi, J. Pu & J. Li.  
37  
38 Preparation and electrochemical properties of  $\text{Li}_{1+x}\text{Al}_x\text{Ge}_{2-x}(\text{PO}_4)_3$  synthesized by a sol-  
39  
40 gel method. *J. Electrochem. Soc.* **2012**, 159 (7), A1114-A1119.  
41  
42  
43 25 H. Morimoto, H. Awano, J. Terashima, Y. Shindo, S. Nakanishi, N. Ito, K. Ishikawa &  
44  
45 S.-i. Tobishima. Preparation of lithium ion conducting solid electrolyte of NASICON-  
46  
47 type  $\text{Li}_{1+x}\text{Al}_x\text{Ti}_{2-x}(\text{PO}_4)_3$  ( $x=0.3$ ) obtained by using the mechanochemical method and  
48  
49 its application as surface modification materials of  $\text{LiCoO}_2$  cathode for lithium cell. *J.*  
50  
51 *Power Sources* **2013**, 240, 636-643.  
52  
53  
54  
55  
56  
57  
58  
59  
60

- 1  
2  
3  
4 26 J. S. Thokchom, N. Gupta & B. Kumar. Superionic conductivity in a lithium aluminum  
5 germanium phosphate glass–ceramic. *J. Electrochem. Soc.* **2008**, *155* (12), A915-A920.  
6  
7  
8 27 N. Imanishi, S. Hasegawa, T. Zhang, A. Hirano, Y. Takeda & O. Yamamoto. Lithium  
9 anode for lithium-air secondary batteries. *J. Power Sources* **2008**, *185* (2), 1392-1397.  
10  
11  
12 28 S. Hasegawa, N. Imanishi, T. Zhang, J. Xie, A. Hirano, Y. Takeda & O. Yamamoto.  
13 Study on lithium/air secondary batteries—stability of NASICON-type lithium ion  
14 conducting glass–ceramics with water. *J. Power Sources* **2009**, *189* (1), 371-377.  
15  
16  
17 29 H. Zhong, L. Sang, F. Ding, J. Song & Y. Mai. Conformation of lithium-aluminium alloy  
18 interphase-layer on lithium metal anode used for solid state batteries. *Electrochim. Acta*  
19 **2018**, *277*, 268-275.  
20  
21  
22 30 B. Wu, S. Wang, J. Lochala, D. Desrochers, B. Liu, W. Zhang, J. Yang & J. Xiao. The  
23 role of the solid electrolyte interphase layer in preventing Li dendrite growth in solid-  
24 state batteries. *Energy Environ. Sci.* **2018**, *11*, 1803-1810.  
25  
26  
27 31 H. Chung & B. Kang. Mechanical and thermal failure induced by contact between a  
28  $\text{Li}_{1.5}\text{Al}_{0.5}\text{Ge}_{1.5}(\text{PO}_4)_3$  solid electrolyte and Li metal in an all solid-state Li cell. *Chem.*  
29 *Mater.* **2017**, *29* (20), 8611-8619.  
30  
31  
32 32 C. Yu, S. Ganapathy, E. R. Van Eck, H. Wang, S. Basak, Z. Li & M. Wagemaker.  
33 Accessing the bottleneck in all-solid state batteries, lithium-ion transport over the solid-  
34 electrolyte-electrode interface. *Nat. Commun.* **2017**, *8* (1), 1086.  
35  
36  
37 33 F. Sun, M. Osenberg, K. Dong, D. Zhou, A. Hilger, C. J. Jafta, S. Risse, Y. Lu, H.  
38 Markötter & I. Manke. Correlating morphological evolution of Li electrodes with  
39 degrading electrochemical performance of Li/LiCoO<sub>2</sub> and Li/S battery systems:  
40  
41  
42  
43  
44  
45  
46  
47  
48  
49  
50  
51  
52  
53  
54  
55  
56  
57  
58  
59  
60

- Investigated by synchrotron x-ray phase contrast tomography. *ACS Energy Lett.* **2018**, 3 (2), 356-365.
- 34 A. Yermukhambetova, C. Tan, S. R. Daemi, Z. Bakenov, J. A. Darr, D. J. Brett & P. R. Shearing. Exploring 3D microstructural evolution in Li-sulfur battery electrodes using in-situ x-ray tomography. *Sci. Rep.* **2016**, 6, 35291.
- 35 O. O. Taiwo, M. Loveridge, S. D. Beattie, D. P. Finegan, R. Bhagat, D. J. Brett & P. R. Shearing. Investigation of cycling-induced microstructural degradation in silicon-based electrodes in lithium-ion batteries using x-ray nanotomography. *Electrochim. Acta* **2017**, 253, 85-92.
- 36 O. O. Taiwo, D. P. Finegan, J. Gelb, C. Holzner, D. J. Brett & P. R. Shearing. The use of contrast enhancement techniques in x-ray imaging of lithium-ion battery electrodes. *Chem. Eng. Sci.* **2016**, 154, 27-33.
- 37 M. Ebner, F. Geldmacher, F. Marone, M. Stampanoni & V. Wood. X-ray tomography of porous, transition metal oxide based lithium ion battery electrodes. *Adv. Energy Mater.* **2013**, 3 (7), 845-850.
- 38 J. Wang, C. Eng, Y.-C. K. Chen-Wiegarth & J. Wang. Probing three-dimensional sodiation-desodiation equilibrium in sodium-ion batteries by in situ hard x-ray nanotomography. *Nat. Commun.* **2015**, 6, 7496.
- 39 M. Ebner, F. Marone, M. Stampanoni & V. Wood. Visualization and quantification of electrochemical and mechanical degradation in Li ion batteries. *Science* **2013**, 342 (6159), 716-720.

- 40 F. Shen, M. B. Dixit, X. Xiao & K. B. Hatzell. Effect of pore connectivity on Li dendrite propagation within LLZO electrolytes observed with synchrotron x-ray tomography. *ACS Energy Lett.* **2018**, 3 (4), 1056-1061.
- 41 W. Zhang, D. Schröder, T. Arlt, I. Manke, R. Koerver, R. Pinedo, D. A. Weber, J. Sann, W. G. Zeier & J. Janek. (Electro)chemical expansion during cycling: Monitoring the pressure changes in operating solid-state lithium batteries. *J. Mater. Chem. A* **2017**, 5 (20), 9929-9936.
- 42 K. Takahashi, J. Ohmura, D. Im, D. Lee, T. Zhang, N. Imanishi, A. Hirano, M. Phillipps, Y. Takeda & O. Yamamoto. A super high lithium ion conducting solid electrolyte of grain boundary modified  $\text{Li}_{1.4}\text{Ti}_{1.6}\text{Al}_{0.4}(\text{PO}_4)_3$ . *J. Electrochem. Soc.* **2012**, 159 (4), A342-A348.
- 43 P. Pietsch & V. Wood. X-ray tomography for lithium ion battery research: A practical guide. *Ann. Rev. Mater. Res.* **2017**, 47, 451-479.
- 44 C. V. Di Leo, E. Rejovitzky & L. Anand. Diffusion–deformation theory for amorphous silicon anodes: The role of plastic deformation on electrochemical performance. *Int. J. Solids Struct.* **2015**, 67-68, 283-296.
- 45 C. V. Di Leo, E. Rejovitzky & L. Anand. A cahn–hilliard-type phase-field theory for species diffusion coupled with large elastic deformations: Application to phase-separating Li-ion electrode materials. *J. Mech. Phys. Solids* **2014**, 70, 1-29.
- 46 E. Rejovitzky, C. V. Di Leo & L. Anand. A theory and a simulation capability for the growth of a solid electrolyte interphase layer at an anode particle in a Li-ion battery. *J. Mech. Phys. Solids* **2015**, 78, 210-230.

- 1  
2  
3 47 M. G. Boebinger, D. Yeh, M. Xu, B. C. Miles, B. Wang, M. Papakyriakou, J. A. Lewis,  
4 N. P. Kondekar, F. J. Q. Cortes, S. Hwang, X. Sang, D. Su, R. R. Unocic, S. Xia, T. Zhu,  
5 M. T. McDowell. Avoiding fracture in a conversion battery material through reaction  
6 with larger ions. *Joule* **2018**, 2 (9), 1783-1799.  
7  
8  
9  
10  
11  
12 48 G. Bucci, T. Swamy, Y.-M. Chiang & W. C. Carter. Modeling of internal mechanical  
13 failure of all-solid-state batteries during electrochemical cycling, and implications for  
14 battery design. *J. Mater. Chem. A* **2017**, 5 (36), 19422-19430.  
15  
16  
17  
18  
19 49 A. F. Bower, P. R. Guduru & V. A. Sethuraman. A finite strain model of stress, diffusion,  
20 plastic flow, and electrochemical reactions in a lithium-ion half-cell. *J. Mech. Phys.*  
21 *Solids* **2011**, 59 (4), 804-828.  
22  
23  
24  
25  
26 50 M. T. McDowell, S. Xia & T. Zhu. The mechanics of large-volume-change  
27 transformations in high-capacity battery materials. *Extreme Mech. Lett.* **2016**, 9, 480-494.  
28  
29  
30  
31 51 S. D. Jackman & R. A. Cutler. Effect of microcracking on ionic conductivity in LATP. *J.*  
32 *Power Sources* **2012**, 218, 65-72.  
33  
34  
35  
36  
37  
38  
39  
40  
41  
42  
43  
44  
45  
46  
47  
48  
49  
50  
51  
52  
53  
54  
55  
56  
57  
58  
59  
60



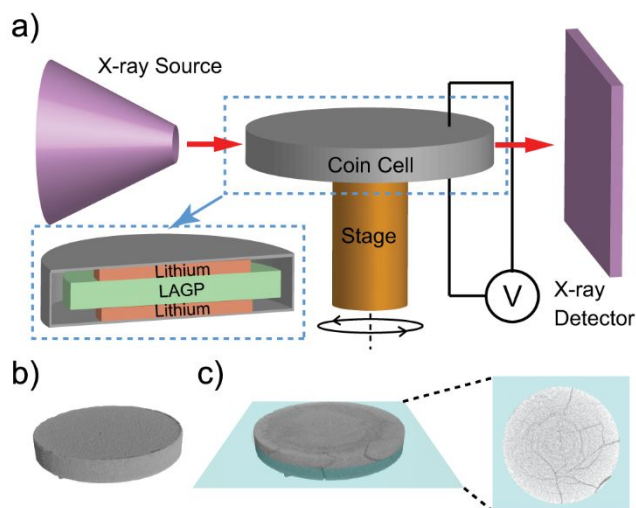


**Figure 1.** a) *In-situ* X-ray micro CT experimental setup for imaging an SSE within a symmetric Li/LAGP/Li coin cell. b) A 3D-rendered volume of a pristine LAGP pellet (8.6 mm diameter) within a symmetric cell before electrochemical cycling. c) A 3D-rendered volume of an LAGP pellet within the same cell after electrochemical cycling. The 2D slice extracted from this image shows that a crack network has grown in the material.

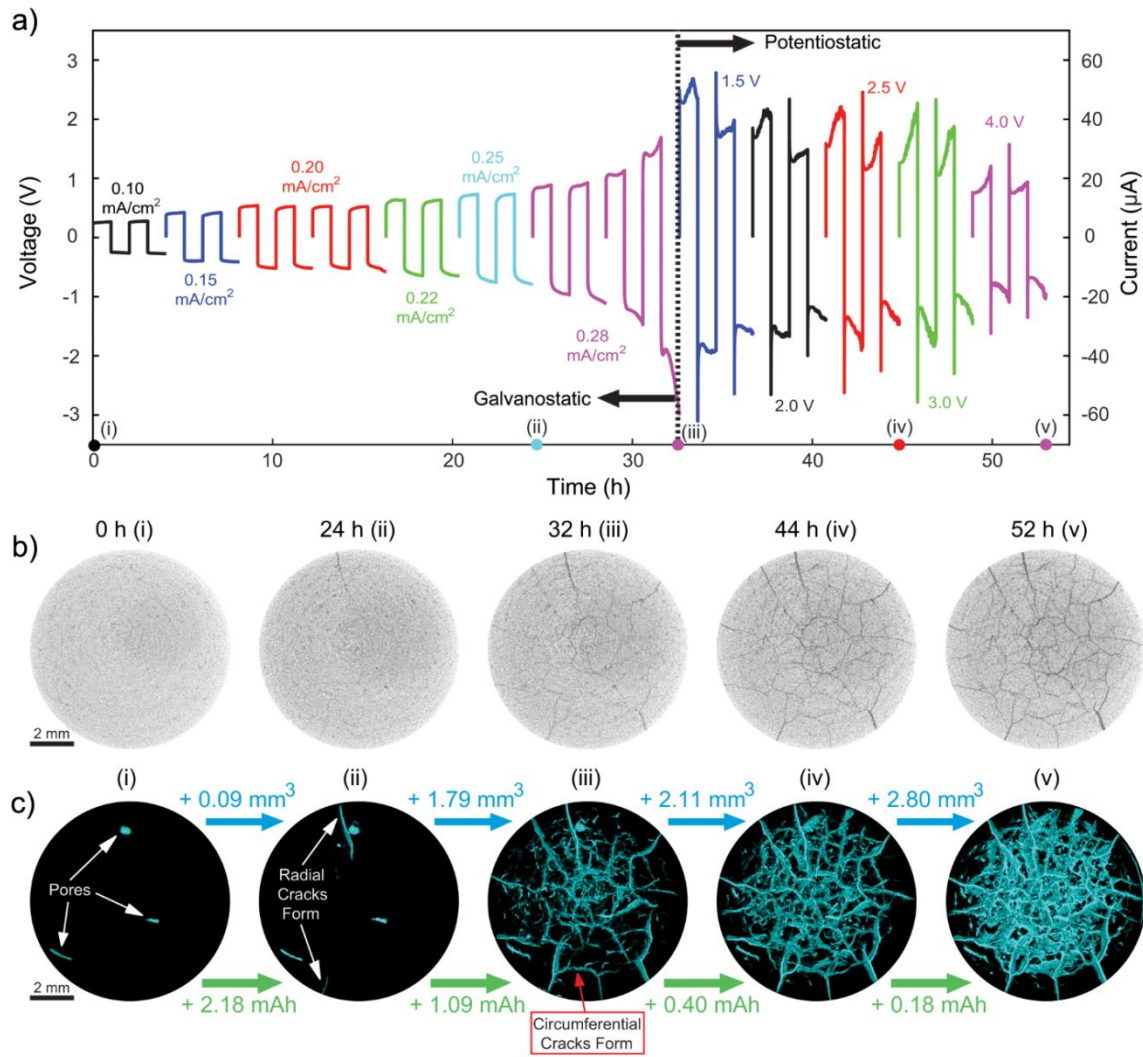


**Figure 2.** Electrochemical data and mechanical degradation of LAGP within a Li/LAGP/Li cell during cycling. **a)** Electrochemical measurement in which galvanostatic cycling at increasing current densities (as labeled) was performed for the first 32 h (the left vertical axis shows corresponding voltages), and then potentiostatic cycling was used for the remaining time (changing cell voltages are also labeled, and the right vertical axis shows corresponding currents). X-ray CT scans were conducted every 4 h of electrochemical cycling, where each new color corresponds to a change in cycling parameters. **b)** 2D slices from the center of the LAGP pellet extracted from the 3D tomogram (i) before electrochemical cycling and after cycling for (ii) 24 h, (iii) 32 h, (iv) 44 h, and (v) 52 h. The dark lines represent cracks within the LAGP pellet, forming a web-like pattern. **c)** 3D crack networks shown throughout the entire LAGP pellet at the same time increments as in (b). The increase in crack volume between these measurements (mm<sup>3</sup>) is shown above the blue arrows between the images, and the amount of charge transferred between measurements (mAh) is shown below the green arrows between images.

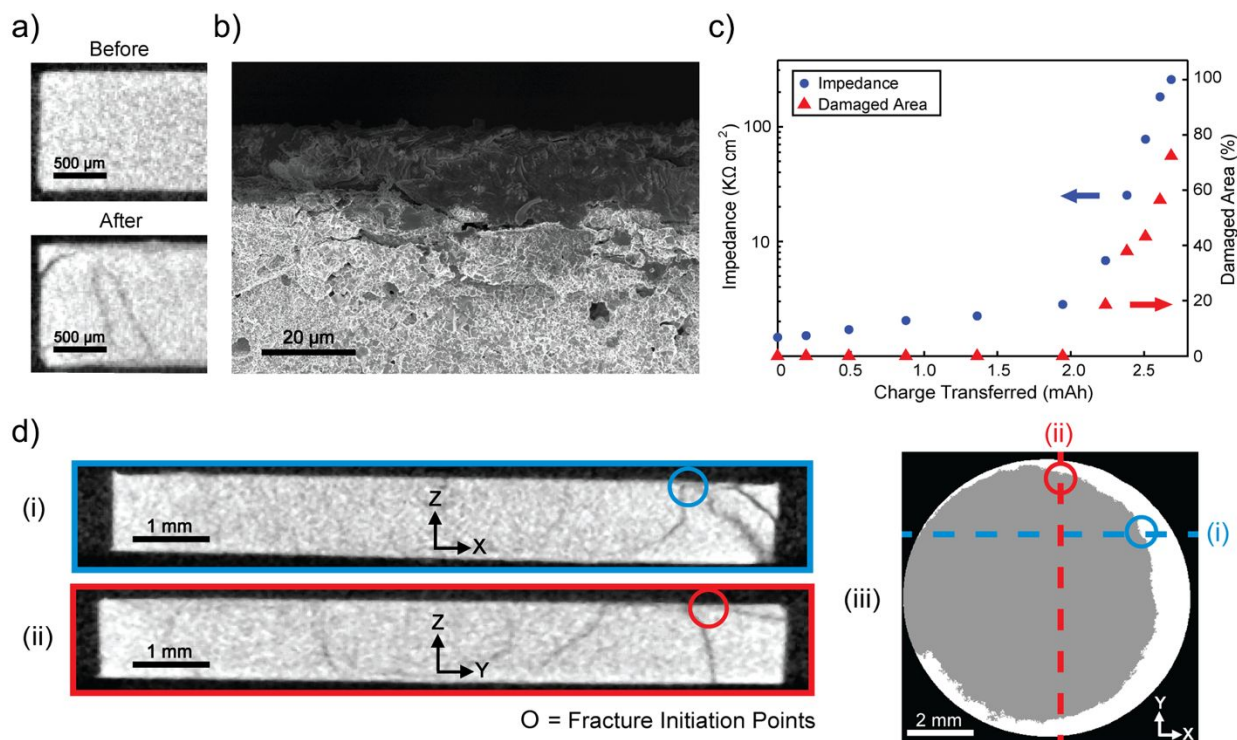


**Figure 3.** *Interphase growth and origin of fracture in LAGP.* **a)** Extracted 2D cross-sectional slices of an LAGP pellet before (top) and after (bottom) undergoing chemical reaction and cycling at low current densities. The formation of a darker region at the Li/LAGP interface after electrochemical treatment signifies the growth of a reacted interphase region. **b)** *Ex-situ* cross-sectional SEM of LAGP cycled at  $0.2 \text{ mA cm}^{-2}$  until failure, where the darker interphase and resultant cracks are clearly visible. **c)** The impedance of a different cell as a function of the total amount of charge transferred. The damaged area, measured as the fractional area with visible cracks in the cross-sectional X-ray images, increases concurrently with the cell impedance. **d)** Cross-sectional image slices with different orientations from the cell in (c) after cycling. The first visible cracks formed at the upper right side of each image at the locations marked with "O." The images in (i) and (ii) are mapped onto the top-down schematic of the full pellet (the white circle) in (iii) with dashed colored lines. The gray shading in (iii) corresponds to the lithium contact area, and the points of fracture initiation seen in (i) and (ii) are again marked with "O." The cracks initiated at the edge of the Li/LAGP contact area.

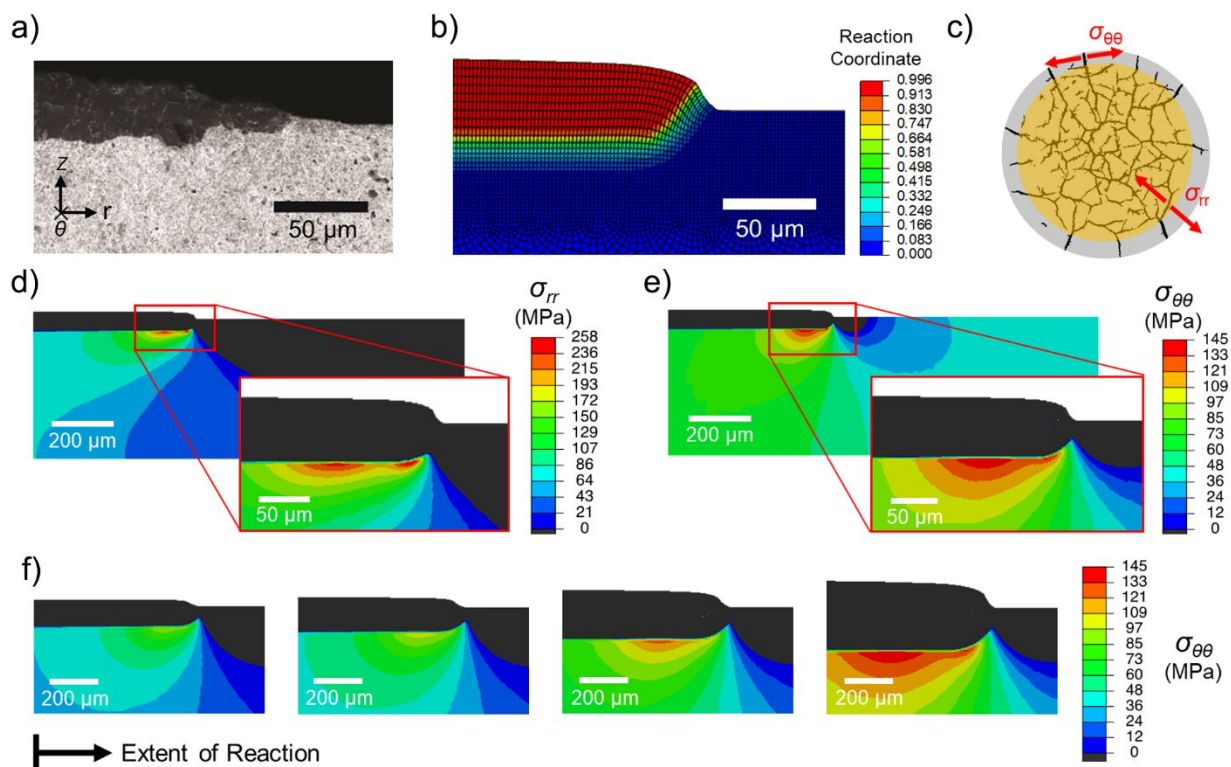


**Figure 4.** Finite element analysis of stress evolution within the SSE due to interphase growth. **a)** Cross-sectional SEM image of an LAGP pellet after being in contact with lithium for  $>100$  h. The lithium foil has been removed, and the darker region at the top of the pellet is the reacted interphase region. The image shows the edge of the reacted interphase region, which only formed under the Li contact area. **b)** Contours of reaction coordinate  $c \in [0,1]$  visualized on the simulated, fully-expanded interphase region. The simulation features a sharp concentration gradient, as observed in (a). **c)** Segmented 2D image slice of a fractured LAGP pellet showing how radial stress ( $\sigma_{rr}$ ) can cause circumferential cracks and circumferential stress ( $\sigma_{\theta\theta}$ ) can cause radial cracks. The yellow shading denotes the approximate region of lithium metal contact with the LAGP. **d)** Radial stress ( $\sigma_{rr}$ ) contours from the simulation; all regions showing compressive (negative)  $\sigma_{rr}$  are shown in black. The magnified region shows radial stress concentrations near the edge of the expanded interphase. **e)** Circumferential stress ( $\sigma_{\theta\theta}$ ) contours from the simulation with compressive stress values shown in black. The magnified region shows circumferential stress concentrations near the edge of the expanded interphase. **f)** Simulated evolution of circumferential stress within the LAGP pellet as the interphase grows in thickness.

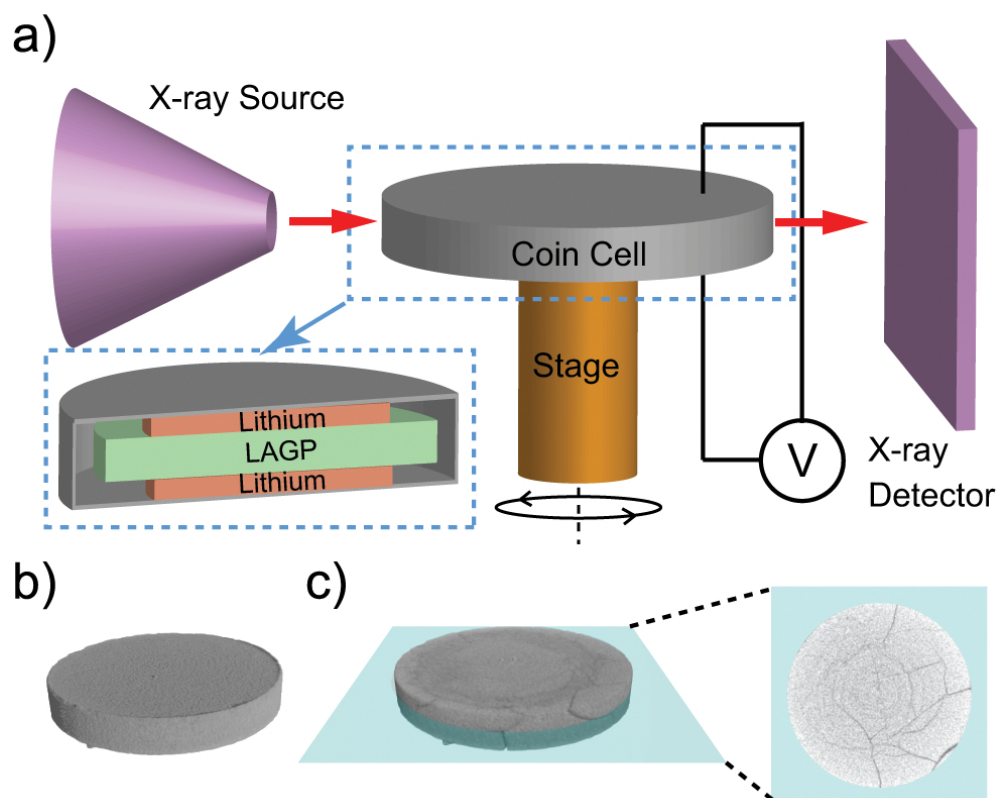


Figure 1

83x69mm (300 x 300 DPI)



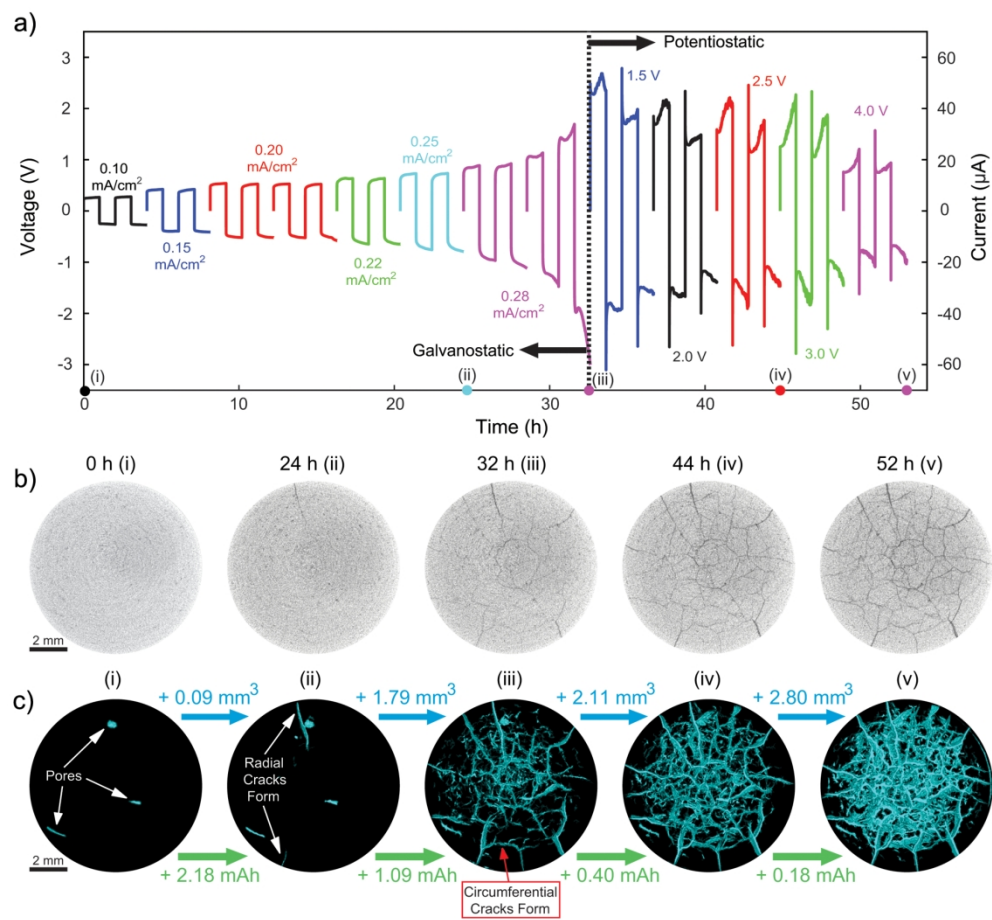


Figure 2

165x151mm (300 x 300 DPI)

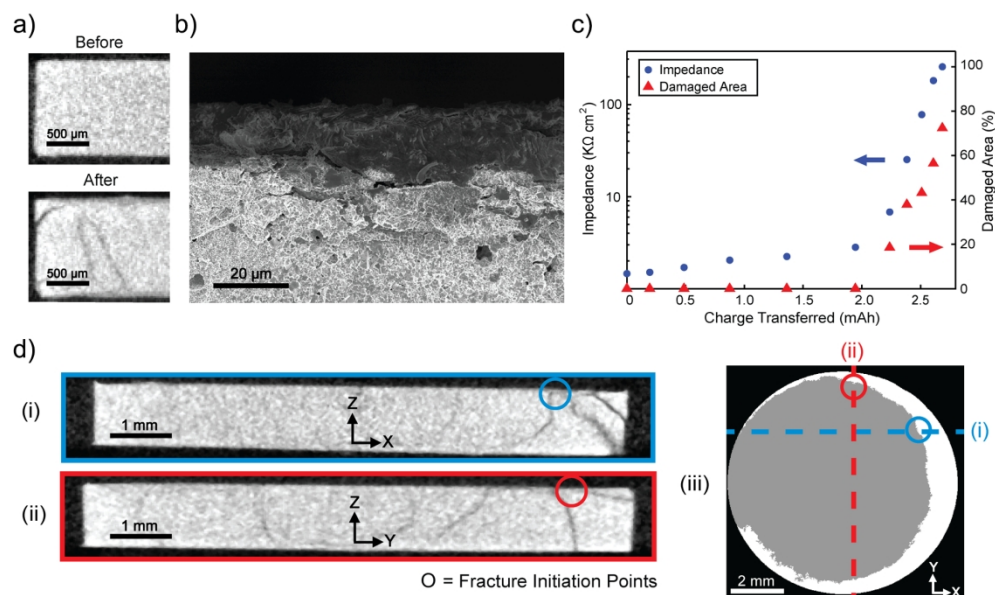


Figure 3

165x97mm (300 x 300 DPI)

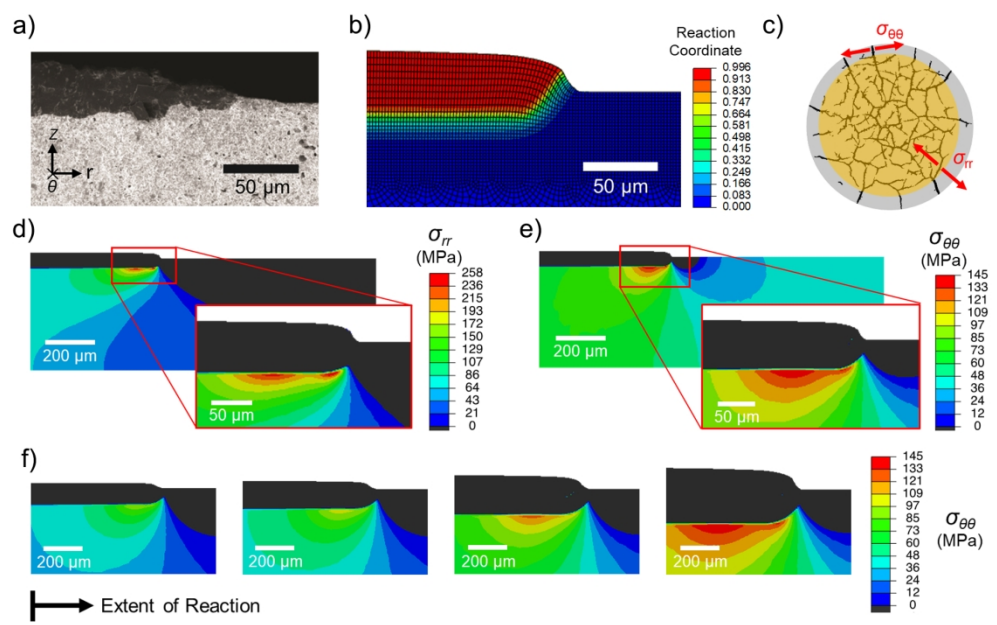
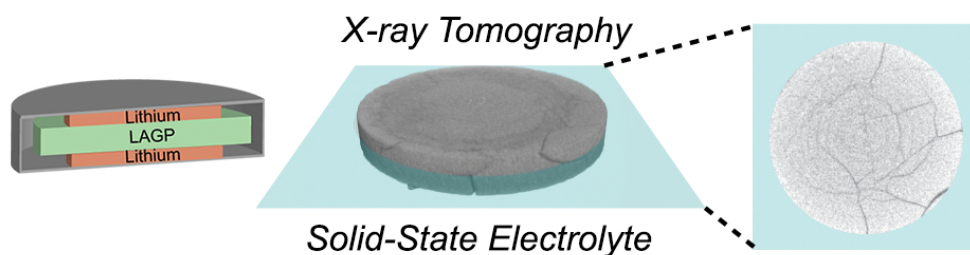


Figure 4





ToC graphic

80x27mm (300 x 300 DPI)